Demonstration of the tunnel-diode effect on an atomic scale

P. Bedrossian*†, D. M. Chen*†‡, K. Mortensen*† & J. A. Golovchenko*†

* Lyman Laboratory, Harvard University, Cambridge, Massachusetts 02138, USA
† Rowland Institute for Science, Cambridge, Massachusetts 02142, USA
‡ Physics Department, University of Western Ontario, London, Ontario, Canada, N6A 3K7

THE tunnel diode[1], which is widely used in high-speed electronics applications[2], depends on the property of negative differential conductivity, that is, a negative slope in the current–voltage curve. The mechanism underlying the tunnel diode's behaviour, namely the existence of a range of biases for which tunnelling is forbidden or suppressed following a bias for which tunnelling is strongly favoured, has been employed subsequently in the design of new devices that also display the conductance anomaly, such as the double-barrier resonant-tunnelling device[3]. It has been predicted[4] that the conductance anomaly could result from a similar mechanism at the tunnel junction of the scanning tunnelling microscope (STM), where localized states on adsorbate and tip atoms give rise to allowed and suppressed energies for tunnelling. The STM has the capability to image regions of negative differential conductivity induced by individual atoms on a surface. Here we report the observation of negative differential conductivity on particular binding sites of a Si (111) surface doped with boron. Specific current–voltage characteristics are shown to be related to the presence or absence of the dopant at individual atomic sites, and negative differential conductivity is observed at −1.4 V tip bias at a specific type of site. Tunnelling spectroscopy indicates that the effect results from a tunnel-diode mechanism.

Samples were prepared by annealing degenerately boron-doped Si (111) crystals (10^{20} cm^{-3}) at 1,000 °C in an ultra-high-vacuum chamber with a base pressure of 10^{-10} torr. This procedure results in boron segregation to the surface[5], with the appearance of the $(\sqrt{3}\times\sqrt{3})$R30° surface periodicity in both low-energy electron diffraction (LEED) and STM. This structure has been established[6] for surface boron concentrations up to one-third of a monolayer (1 monolayer = 7.8×10^{14} atoms cm^{-2}) although it is not characteristic of the pure crystal, where the 7×7 reconstruction is the more stable[7].

Figure 1*a* shows a typical tunnelling image of the boron-doped surface, with individual adatoms spaced 6.7 Å apart. Two types of adatom sites, apparently randomly distributed, are distinguished by their relative brightness in the tunnelling image, and this preparation typically results in the incorporation of 15–20% 'bright' sites in the surface. We have previously established (ref. 8; see also refs 9, 10) that all imaged adatoms are silicon, but with the dark adatom sites sitting directly above a substitutional boron atom and the bright adatom sites above a silicon atom. The surface boron concentration for such a sample, then, is within 20% of saturation at one-third of a monolayer. We shall refer to the lateral locations of the two types of silicon adatom sites as boron-occupied and boron-free positions, respectively. Similar results were obtained after ion-beam sputter deposition of boron onto clean, arsenic-doped (0.02 Ω cm) Si (111), with the surface boron concentration controlled in that case by adjusting the deposition time.

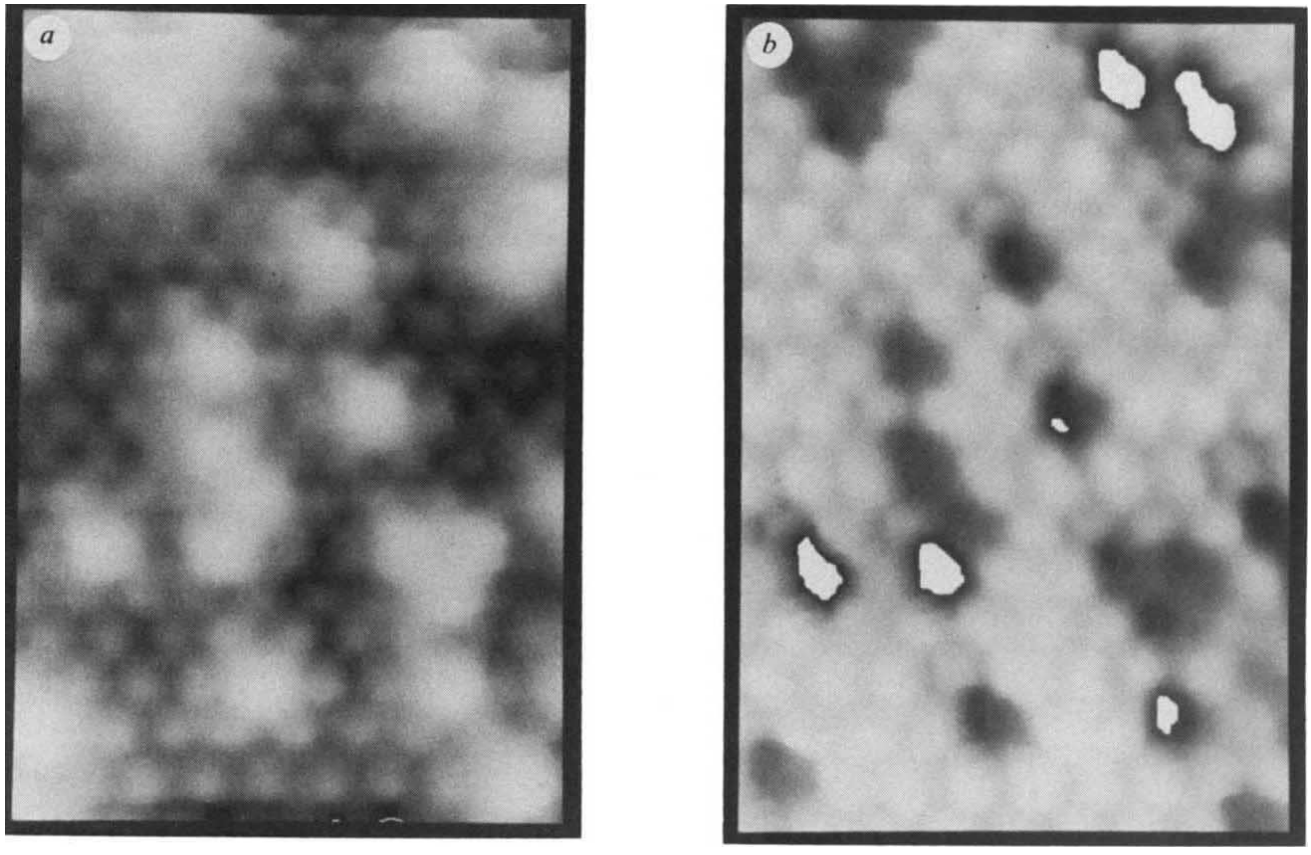

FIG. 1 *a*, 60×170 Å topographical tunnelling image of the Si (111) $(\sqrt{3}\times\sqrt{3})$R30°–B surface prepared by annealling heavily boron-doped Si (111). Tip bias, −1.4 V, 1 nA. The protrusions represent individual atoms. *b*, Image of the differential conductivity at −1.4 V for the region in *a*. Brighter shading indicates higher differential conductivity. The white, highlighted regions indicate negative differential conductivity.

Having identified the two types of adatom sites observed, we can measure atom-resolved current-voltage (I–V) characteristics by sweeping the tip bias and recording the current at the crystal for a particular lateral tip position and fixed tip–sample separation. Many boron-free positions that are immediately adjacent to several boron-occupied positions exhibit negative differential conductivity at a tip-to-sample bias of −1.4 V, as shown in Fig. 2. The conductance anomaly is stable and repeatable, both for individual atomic sites and from one sample to the next. No such feature is observed for boron-occupied positions, or in large regions of boron-free sites.

The spatial distribution of the regions of negative differential conductivity is displayed in an image of the differential conductivity at −1.4 V, which we obtained by placing a 6.25 kHz, 20-mV r.m.s. modulation on the tip bias and recording the output of a lock-in amplifier that senses the sample current signal as a function of lateral position. The modulation frequency is placed outside the bandwidth of the feedback network that adjusts the vertical position of the tip and maintains a constant d.c. tunnelling current. Figure 1*b* displays such an image, corresponding to the region of the surface shown in the topographical image of Fig. 1*a*. In Fig. 1*b*, brighter shading indicates higher differential conductivity, and the solid white areas indicate negative differential conductivity. Comparison with Fig. 1*a* shows that regions of negative differential conductivity are localized on isolated boron-free sites and therefore act as individual tunnel diodes in concert with the STM tip. We note that the surface preparation that gave rise to this behaviour typically results in an average of at least one tunnel diode in a 60×60 Å region.

The mechanism and conditions behind the appearance of the conductance anomaly in this system are indicated by local tunnelling spectra, which are obtained by positioning the tip over an adatom site, fixing the lateral and vertical tip positions momentarily, sweeping the tip bias, and recording the differential conductivity as a function of this bias. When the resulting data are normalized to the total conductivity, as in Fig. 3, peaks in such spectra indicate[11] the presence of a surface state at the energy corresponding to the bias voltage. Negative tip bias corresponds to tunnelling into unoccupied sample states. Thus, an unoccupied state 0.6 eV above the Fermi level is found on boron-free sites but is absent from the boron-occupied positions. The occurrence of such a state at this energy is consistent with the presence of a dangling orbital on Si adatoms that was predicted[12] for clean Si (111) $(\sqrt{3}\times\sqrt{3})$R30° and which has been observed[13] on Si (111) 7×7. Above this bias, the local density of states on boron-free sites falls smoothly for 0.8 eV.

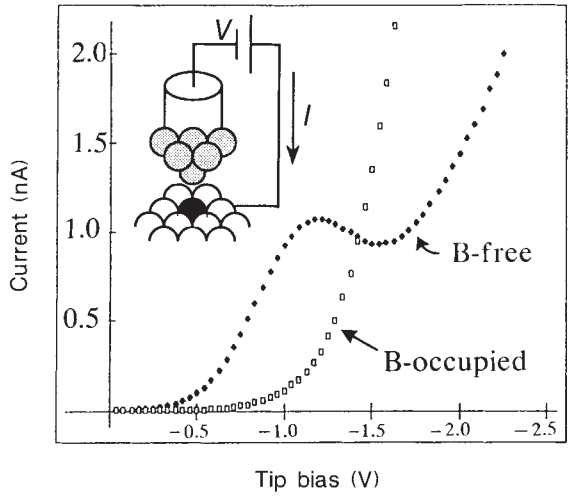

FIG. 2 I–V curves for the case of negative tip bias, acquired with the tip over boron-occupied and boron-free sites in regions of substantial mixing of the two types of sites. Inset, geometry of the tunnelling device.

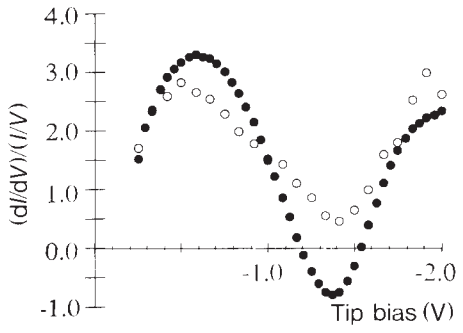

FIG. 3 Tunnelling spectra for the case of negative tip bias, acquired with the tip held over (curve *a*), a boron-free site surrounded by boron-free sites, and (curve *b*), an isolated boron-free site. The presence of the dopant leads to the negative region in curve *b*.

The onset of negative differential conductivity in both the tunnel diode and resonant tunnelling devices has been shown to result from a sharp drop in the tunnelling probability when the bias reaches an energy level at which tunnelling is forbidden. In the former case the forbidden energies lie in the band gap of a degenerate semiconductor; in the latter, between the discretely quantized energy levels in a potential well. In the case we consider, Fig. 3 shows that the differential conductivity at −1.4 V tip bias is low, but non-negative, even in the absence of boron. We expect the lateral isolation of a boron-free site surrounded predominantly by boron-occupied positions to narrow the dispersion of the low-lying silicon dangling-bond state, further reducing the tunnelling probability at −1.4 V bias and meeting the criterion for the conductance anomaly. The tunnel-diode-like I–V curve in Fig. 2 therefore results from a small perturbation in the surface band structure of clean Si, induced by the presence of dopant atoms below adjacent sites.

The mechanism suggested by the above data for the conductance anomaly that we observe should be distinguished from switching behaviour at electron trapping sites, which was shown[14] to be responsible for time-averaged negative resistance at a variety of bias conditions in an STM study of a different system that did not display a unique dangling-bond defect. For that mechanism, switching noise in the tunnelling current was reported[15] within several nanometres of the trapping site. We have not detected similar current fluctuations in the Si (111) $(\sqrt{3}\times\sqrt{3})$R30°-B system, and we do not expect them if the conductance anomaly arises from the tunnel-diode mechanism.

Negative resistance itself can undoubtedly be realized in the STM with other systems under varying degrees of characterization and controllability of the tip and sample. Our data indicate that a particular surface can be characterized sufficiently by STM to apply a principle known to underly the operation of a macroscopic device, specifically the tunnel diode, to engineer I–V characteristics of the tunnel junction of the STM on an atomic scale. The surface states responsible for the I–V characteristics and the nature of the atomic sites at the surface could be identified, and the overall density of tunnel diodes on the surface could be controlled, by adjusting the surface dopant concentration. Although the local dopant distribution resulting from our preparations is a product of random diffusion processes, it can be determined and selected under the STM. The recent achievement[16] of large-scale integration (LSI) of STMs on a Si wafer therefore offers the means to incorporate the microscopic tunnel diode described here in a practical device. □

Received 18 April; accepted 17 October 1989.

1. Esaki, L. *Phys. Rev.* **109**, 603–604 (1958).
2. Sze, S. M. *The Physics of Semiconductor Devices* Ch. 9 (Wiley, New York, 1981).
3. Esaki, L. *Rev. Mod. Phys.* **36**, 237–244 (1974).

4. Lang, N. D. *Phys. Rev.* B**34,** 5947–5950 (1986).
5. Korobtsov, V. V., Lifshits, V. G. & Zotov, V. G. *Surf. Sci.* **195,** 466–474 (1988).
6. Hirayama, H., Tatsumi, T. & Aizaki, N. *Surf. Sci.* **193,** L47–L52 (1988).
7. Takayanagi, K., Tanishiro, Y., Takahashi, M. & Takahashi, S. *J. Vac. Sci. Technol.* A**3,** 1502–1506 (1985).
8. Bedrossian, P. *et al. Phys. Rev. Lett.* **63,** 1257–1260 (1989).
9. Headrick, R. L., Robinson, I. K., Vlieg, E. & Feldman, L. C. *Phys. Rev. Lett.* **63,** 1253–1256 (1989).
10. Lyo, I.-W., Kaxiras, E. & Avouris, P. *Phys. Rev. Lett.* **63,** 1261–1264 (1989).
11. Feenstra, R., Stroscio, J. & Fein, A. *Surf. Sci.* **181,** 295–306 (1987).
12. Northrup, J. *Phys. Rev. Lett.* **57,** 154–157 (1986).
13. Nicholls, J. & Reihl, B. *Phys. Rev.* B**36,** 8071–8074 (1987).
14. Hamers, R. & Koch, R. in *The Physics and Chemistry of SiO_2 and the Si-SiO_2 Interface* (eds Helms, C. & Deal, B.) 201–210 (Plenum, New York, 1988).
15. Welland, M. & Koch, R. *Appl. Phys. Lett.* **48,** 724–726 (1986).
16. Petit, C. *Mosaic* **20,** 24–35 (1989).

ACKNOWLEDGEMENTS. This work was supported by the Office of Naval Research and the Joint Services Electronics Program.

Determination of 4-connected framework crystal structures by simulated annealing

M. W. Deem & J. M. Newsam

Exxon Research and Engineering Company, Route 22 East, Annandale, New Jersey, USA

THE initial derivation of atomic-scale models of the 4-connected framework crystal structures of zeolites and related materials is generally difficult. Interpretation of powder X-ray diffraction data to yield a unit cell and some symmetry information is often straightforward. Chemical analyses and sorption experiments indicate the number of framework tetrahedra, n_T, present in the unit cell (T represents the framework tetrahedral species, such as Si or Al) and the approximate pore dimensions. However, because synthetic zeolites are almost invariably microcrystalline, the possibilities for structure solution by conventional diffraction methods are limited, and framework structure determinations have traditionally relied heavily on the building of physical models. We describe here an alternative approach, in which approximate T-atom coordinates are derived from the unit-cell size and symmetry, and the value of n_T from computer modelling. An initially arbitrary T-atom configuration is optimized with respect to a 'cost function' based on the T–T distances, T–T–T angles and number of first-neighbour T-atoms, by simulated annealing using Monte Carlo methods. The potential of the method for structural determinations in both two dimensions (for structural projections) and three dimensions are illustrated by results obtained for a hexagonal cell of space group *P6/mmm* and dimensions $a = 18.4$ Å and $c = 7.5$ Å, and by determination of the previously unknown structure of lithium gallosilicate.

A large proportion of the ~65 known zeolite framework structure types[1] were solved based on an initial determination of the 4-connected T-atom framework by, for example, physical model building[2], by consideration of direct derivatives of known structures[3], or by interpretation of electron microscopy and diffraction data[4,5]. Oxygen atoms can be added at the midpoints of each of the T–T vectors, and the T- and O-atom coordinates then optimized readily by distance least-squares (DLS) based on established constraints on the T–O, O–O and T–T distances[6,7]. The problem of structure solution reduces to one of defining approximate T-atom coordinates. The present approach describes the reasonableness of a given arrangment of the required number of T-atoms in the known unit cell in terms of a cost or 'energy' function and uses simulated annealing to adjust the T-atom coordinates to minimize that energy.

We define the total energy of a given T-atom configuration as the sum over the unique T-atoms of terms based on the T–T distances, T–T–T angles, the number, N_1, of first neighbours, and (when T-atoms are possibly located on symmetry elements) the number of symmetry operations that reproduce the original T-atom (Fig. 1). The forms of the energy as a function of the T–T distances and of the T–T–T angles are derived from histograms of observed data from a representative number of known zeolite structure types. The neighbour term is calculated from the number of T-atoms within a defined shell. The merging contribution is calculated from the distance between symmetry-related T-atoms found at less than a defined separation; merged atoms are excluded from the calculations of the other energy terms. Merging is permitted provided the total number of T-atoms per unit cell is $\geq n_T$. Appropriate relative weights of the four types of constraint were derived largely by trial and error, with the parameters being treated as tunable in complicated cases. Appropriate adjustment of these various terms (particularly the neighbour term) permits the same method to be applied to other coordination environments such as those that occur, for example, in mixed octahedral–tetrahedral framework structures.

Optimization of the coordinates of the unique T-atoms (the full unit-cell T-atom complement is generated by application of the space-group operators) to minimize the calculated energy sum is achieved by Monte Carlo methods using simulated annealing[8,9] based on an initially random configuration. During annealing low-energy, 4-connected configurations generated are stored for further evaluation (typically, 2–20 are produced in each run). Simple representations (projections down the three principal crystallographic directions) of the full unit-cell contents for each of the saved models are examined visually, followed, where appropriate, by further molecular graphics analyses, or by addition of framework oxygen atoms and DLS optimization and/or simulation of the powder-X-ray diffraction pattern(s). A typical run for a three-dimensional case (see below) with $n_{unique} = 2$ unique T-sites, 24 symmetry operators and $n_T = 36$ consumes ~60 min CPU time on a VAX8350, or ~60 s on a Cray XMP/14 se.

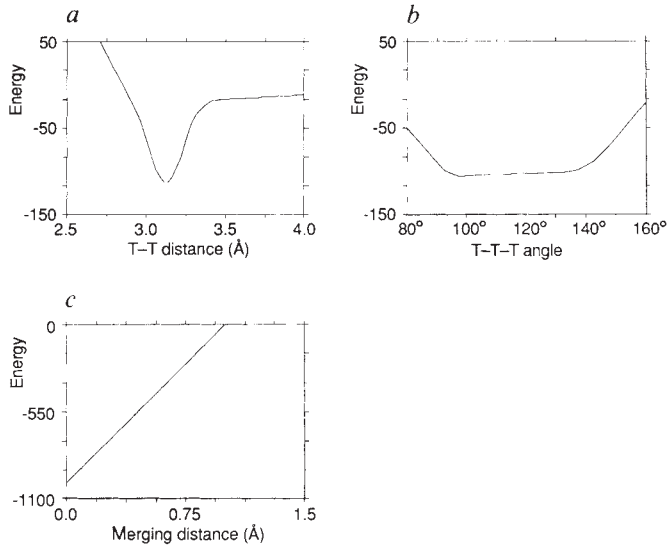

FIG. 1 Energy as a function of the T–T distance (*a*) and the T–T–T angle (*b*) used in the simulation procedure (calculated as smoothing spline fits to Boltzman equilibrium interpretations of histogrammed data taken from 32 representative zeolite crystal structures). Only the central portions are shown, the energy curves extrapolating linearly to energies of 1,000.0 and 0.0 at T–T distances of 0.0 and 5.0 Å, and to energies of 5,000.0 and 0.0 at T–T–T angles of 0.0 and 180° respectively. (*c*) The contribution to the energy sum for the merging of two symmetry-related atoms; merging is only permitted when the two atoms are at less than a defined minimum distance. The contribution to the energy sum from the coordination term is typically set to 1,000.0, 800.0, 600.0, 300.0, 0.0, 300.0, 600.0 for 0, 1, 2, 3, 4, 5 and 6 T-atoms within the defined first-neighbour radius (typically 3.7 Å) respectively.